

Robust aluminum nitride passivation of silicon carbide with near-surface spin defects

Cyrille Armel Sayou Ngomsi¹ and Pratibha Dev¹

¹*Department of Physics and Astronomy, Howard University, Washington, D.C. 20059, USA*

Silicon carbide (SiC) hosts a number of point defects that are being explored as single-photon emitters for quantum applications. Unfortunately, these quantum emitters lose their photostability when placed in proximity to the surface of the host semiconductor. In principle, a uniform passivation of the surface's dangling bonds by simple adsorbates, such as hydrogen or mixed hydrogen/hydroxyl groups, should remove detrimental surface effects. However, the usefulness of atomic and molecular passivation schemes is limited by their lack of long-term chemical and/or thermal stability. In this first principles work, we use aluminum nitride (AlN) to passivate SiC surfaces in a core-shell nanowire model. By using a negatively charged silicon vacancy in SiC as the proof-of-principle quantum emitter, we show that AlN-passivation is effective in removing SiC surface states from the band gap and in restoring the defect's optical properties. We also report the existence of novel silicon vacancy-based defects at the SiC-AlN interface.

INTRODUCTION

Quantum bits (qubits) and single photon emitters are essential building blocks for quantum information science applications. Wide band gap semiconductors with fluorescent, spin-active point defects can furnish both qubits and single photon emitters for quantum technologies. This is particularly true for different bright defects in silicon carbide (SiC), which not only emit single photons in the favorable near-telecom range [1, 2], but they also possess addressable spins [3–6] with long coherence times [1, 4–7]. The host material itself offers additional advantages, such as low cost, commercial availability, and ease of nanofabrication, all of which can enable scalable SiC-based quantum technologies.

In order to enhance the radiative signal from defects for quantum computing and/or enhance their sensitivity for quantum sensing applications, different strategies are used, such as shallow implantation and/or nanofabrication of optical cavities in the host materials [8–14]. A consequence of these strategies is the near-surface placement of the defect, which inadvertently modulates its properties. This has been reported in experiments [13, 15–18] and explored in a few theoretical works [19–23]. In particular, two recent theoretical works [22, 23] studied properties of the near-surface, negatively-charged silicon monovacancy (V_{Si}^{-1}) in a 2H-SiC nanowire (NW). In their first principles study of defects in an unpassivated NW, Joshi and Dev [22] demonstrated that the changes to the frequency of quantum emission from V_{Si}^{-1} and the loss of the defect's photostability result from the spatial and energetic proximity of the surface states to the defect states. Sayou Ngomsi *et al.* [23] further showed that the aforementioned detrimental surface effects can be remedied by passivation of the SiC surfaces with simple adsorbates, such as hydrogen or mixed hydrogen/hydroxyl groups. The resulting removal of the SiC surface states from the band gap leads to a near-perfect restoration of the defect's emission frequency and its photostability by the elimination of different charge-conversion pathways.

Although effective and experimentally straightforward to implement, the use of atomic and molecular adsorbates is limited by their thermal and chemical stability in the long-term [24, 25]. Hence, a more robust passivation scheme is needed that retains the different benefits of using simple adsorbates, but eliminates their limitations. That this can be achieved was shown in an experimental work by Polking *et al.* [26]. The authors grew an epitaxial layer of wurtzite aluminum nitride (AlN) on a SiC surface and reported improved photostability of the positively-charged carbon antisite-vacancy defect complexes within SiC. These were promising experimental results, however, to date, there are no theoretical studies to explain how AlN passivation restores a defect's photostability, or its effects on other SiC defects. For example, it is not known if such a passivation scheme will also improve the charge-state stability of the silicon monovacancy, which is bright only in the negatively charged state. In this first principles work, we study AlN-coverage of SiC surfaces by modeling a core-shell nanowire with a SiC core and an AlN shell. Using V_{Si}^{-1} in SiC as a proof-of-principle defect, we demonstrate that AlN effectively removes SiC surface states from the band gap, restoring the defect's optical properties. We also report the existence of novel silicon vacancy-based defects at the SiC-AlN interface with distinct spin and optical properties.

COMPUTATIONAL METHODS

Our density functional theory (DFT)-based spin-polarized calculations were performed using the QUANTUM ESPRESSO package [27, 28]. We used ultrasoft pseudopotentials [29], which allow for low energy cut-offs of 50 Ry for expanding wave functions and 350 Ry for charge densities. In addition, all of the results reported in this work are for structures that were relaxed until the forces on the atoms were smaller than 10^{-3} Ry/a.u. We used the generalized gradient potential approximation (GGA) [30] of Perdew, Burke, and Ernzerhof (PBE) [31]

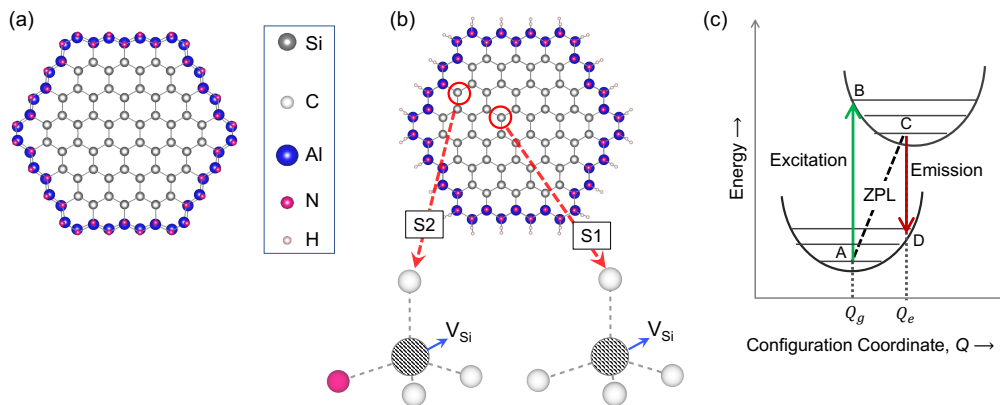


FIG. 1. Aluminum nitride passivated silicon carbide nanowire (NW). (a) SiC/AlN NW (cross-sectional view), (b) Hydrogen (-H) terminated SiC/AlN NW to mimic a thicker AlN shell (cross-sectional view). Passivation of SiC core with AlN shell creates two distinct defect sites (S1 and S2) relative to the interface between SiC core and AlN shell. (c) Franck-Condon picture used for interpreting Δ SCF results.

to account for the exchange-correlation effects. It should be added here that we chose to use PBE functional instead of computationally expensive hybrid functionals, such as HSE06 [32, 33]. The latter functionals are known to correct for the underestimation of band gaps within PBE [34]. However, in the present study, we chose PBE functional because: (a) it made our calculations for large nanostructures feasible, and (ii) in our nanostructures, the PBE-related underestimation of band gaps is compensated by the quantum confinement effects that come into play in nanostructures that result in larger band gaps. This compensation ensures a correct placement of defect states in the band gap and hence, to accurate values for quantum emission frequencies.

Our structure is a core-shell NW with a 2H-SiC polytype at its core and a shell of wurtzite AlN. As done in recent studies [22, 23], we chose to use the 2H-SiC polytype for the NW because it ensured that the as-created stoichiometric nanostructures were non-magnetic, with no magnetic moment on any atom. This prevented any surface-related spin from interacting with the spin of V_{Si}^{-1} , allowing us to concentrate on the role that the finite-size and surface effects play in modifying the defect's properties. Our calculations show the bulk lattice constants, a (in-plane) and c (out-of-plane) of wurtzite AlN and 2H-SiC differ by 1.3% and 2.3%, respectively. Hence, wurtzite AlN is a good choice for the passivation layer due to its small lattice-mismatch with 2H-SiC. The ideal unpassivated SiC/AlN NW, shown in Fig. 1(a), has a diameter of 21.8 Å. The NW is periodic along the [0001] direction (c -axis), with a vacuum of about 13.5 Å separating the images of the NW in the lateral direction (perpendicular to the c -axis), minimizing the interaction between the periodic images of the nanowire. We use a gamma-centered k -point grid of $1 \times 1 \times 6$, created according to the Monkhorst-Pack scheme [35]. The unpassivated core-shell NW (from here on, called SiC/AlN NW)

has a total of 384 atoms, with a SiC core of 216 atoms and an AlN shell consisting of 168 atoms. The SiC/AlN NW was further passivated with hydrogen for reasons that will be discussed in the next section. It is this passivated core-shell structure (SiC/AlN-H NW) that was used in our study. Figure 1(b) shows the cross-sectional view of the SiC/AlN-H NW with a total of 480 atoms. There are two distinct possibilities for the placement of silicon monovacancies relative to the interface between SiC and AlN: within the SiC core (i.e. away from the interface) or at the interface itself. Two such sites – S1 and S2 – are shown in Figure 1(b). In this work, we used silicon vacancies at these sites to determine the efficacy of AlN in removing dangling bonds and restoring the optical properties of the monovacancies. Since the hydrogen-passivated SiC NW used in the older work by Sayou *et al.* [23] had a smaller diameter, we performed additional calculations for a hydrogen-passivated SiC NW (henceforth, called SiC-H NW), consisting of 480 atoms for the sake of direct comparison with the results for defects in SiC/AlN-H NW.

In order to study the optical properties of the near-surface V_{Si}^{-1} in SiC/AlN-H NW, we obtained the zero-phonon line (ZPL) using the Δ SCF method [36], which has been successfully employed to study excitations between spatially-localized defect states of deep-level defects in different wide band gap semiconductors [22, 23, 37, 38]. In the Δ SCF method, the occupation of the defect states is constrained to mimic the photo-excitation process as described within the Franck-Condon model shown in Fig. 1(c). Point A in the Franck-Condon picture represents the system in the electronic ground state with the ground-state equilibrium ionic positions (generalized coordinate Q_g). The spin-preserving, vertical optical excitation, $A \rightarrow B$, involves emptying of a filled defect state and the simultaneous occupation of the previously empty defect state (without structural relaxation). Point C in

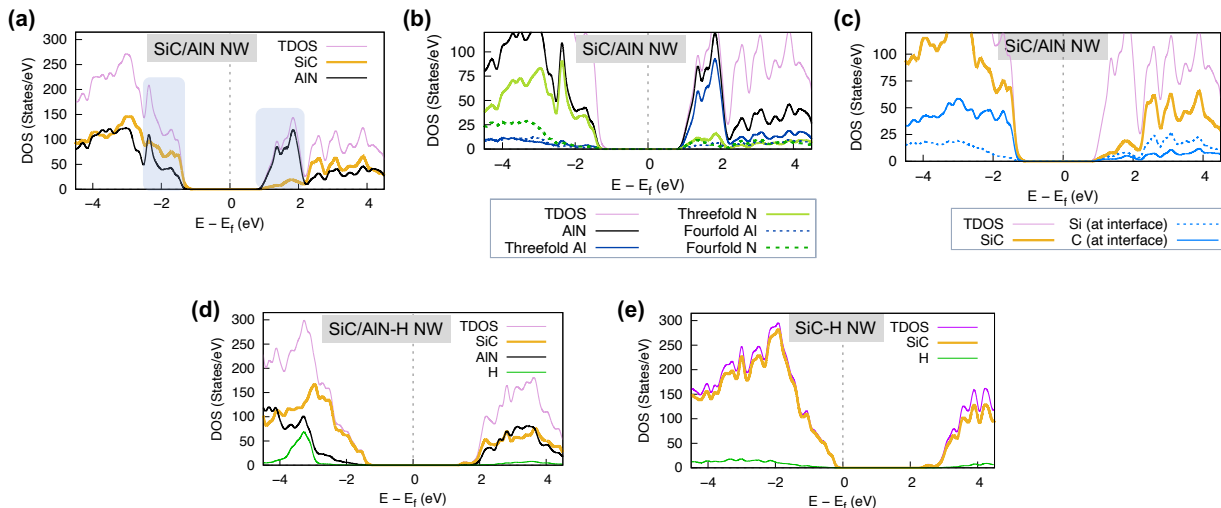


FIG. 2. Electronic structure properties of defect-free 2H-SiC NWs. (a) Total and projected density of states (DOS) for unpassivated/bare SiC/AlN NW, showing the narrowing of the bandgap in the core-shell structure to 2.17 eV due to surface and interface states (highlighted in blue). (b) DOS projected onto the threefold and fourfold coordinated Al and N atoms in the AlN shell, showing their contribution to the states at the band edges of the bare core-shell NW. (c) DOS projected onto the Si and C atoms at the interface between the core-shell NW, showing contributions from the interfacial carbons to the DOS at the valence band edge. (d) The surface and interface states are removed by hydrogenation of the core-shell NW. (e) DOS for SiC-H NW for comparison.

the Franck-Condon picture is accessed by allowing for the ionic relaxation (excited-state generalized coordinate Q_e) that follows the new electronic configuration in the excited-state. Point D corresponds to the system with excited-state ionic positions, Q_e , and ground state electronic configuration. The total energy differences for the system at points A , B , C and D yield the following: (i) vertical transition upon absorption of a photon ($A \rightarrow B$), (ii) purely electronic ZPL transition ($A \leftrightarrow C$), (iii) the Stokes shift ($B \rightarrow C$) and (iv) the vertical de-excitation upon emission of a photon ($C \rightarrow D$).

RESULTS AND DISCUSSION

Defect-free Core-Shell NW

The spatial and energetic proximity of the surface states to the defect states allows them to interfere with the photostability of the quantum emitters [22, 23]. This can be avoided by passivating SiC dangling bonds within the passivation-scheme of choice, be it simple adsorbates or a coverage with another semiconductor. In principle, with the AlN-passivation of SiC one should obtain an electronic structure where the surface-states from the AlN shell are far removed from defect states (at least spatially). However, as can be seen in the density of states (DOS) plot in Fig 2(a) for the bare/unpassivated SiC/AlN NW, we have surface states in the band gap. Figures 2(b) and (c) plot the DOS projected onto the $2s$ and $2p$ orbitals of atoms belonging to the AlN shell and

the interfacial Si and C atoms of the SiC core. A closer look at the two figures shows that it is the threefold-coordinated Al and N atoms, along with the C atoms at the interface that contribute the most to the states at the band edges of the core-shell NW. One expects to find the surface states originating from threefold-coordinated Al and N atoms at the band edges [23]. However, the reasons for the presence of the states from the interfacial C atoms at the band edges are not self-evident. For this, we need to consider the skin-bond contraction effect, which is found in very small nanostructures [39]. The skin contraction occurs due to the strengthening of the bonds at the undercoordinated surface sites, which aids in a reduction of the surface energy. The outcome of the bond-contraction is evident in Fig. 1(a), which shows a marked change of hybridization from the ideal sp^3 to a mixed sp^2 - sp^3 type for the surface atoms [compare with Fig. 1(b)]. These structural changes at the surface propagate to the interior of the NW [22, 23]. Since we have a thinner shell, these structural changes at the AlN surface propagate to the SiC-AlN interface, affecting the structure of SiC at the interface. The presence of surface states and the states from the interfacial atoms, in turn, reduces the band gap of the SiC/AlN NW to 2.17 eV, which is smaller than the theoretical band gap (2.31 eV) of bulk 2H-SiC. The calculated electronic structure of the SiC/AlN NW are an artifact of our core-shell model, in which the AlN shell is extremely thin. However, in order to demonstrate that AlN grown on SiC is an effective passivation scheme for improving optical properties of near-surface defects, it should be shown that the

hybridization between the detrimental surface states and the defect states from V_{Si}^{-1} in SiC is minimal. This can be achieved only if the defect states are energetically and/or spatially far removed from surface states. In other words, we need to either create a structure with much thicker shell or a structure that mimics the behavior of a thicker shell. Due to the prohibitive cost of calculations involving thicker shells, we decided to emulate a much thicker AlN shell by passivating the structure with hydrogen. A full hydrogen coverage of all threefold coordinated surface atoms (totaling 96 atoms) removed the detrimental surface and interfacial states from the band edges as seen in Fig. 2(d). As a consequence, the band gap of the resulting SiC/AlN-H NW is 2.85 eV. As expected, this is larger than the band gap for the bulk material due to quantum confinement effects that come into play in a nanostructure. For comparison, we also plot the DOS of the SiC-H NW, which shows a band gap of 2.77 eV.

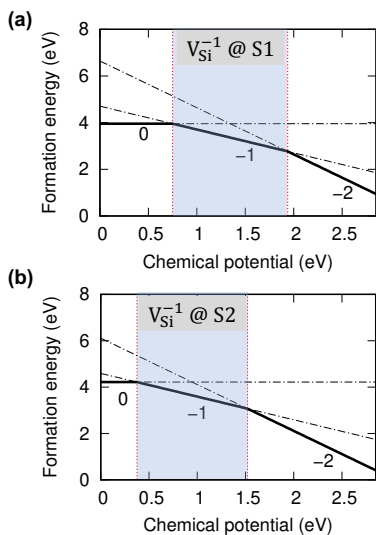


FIG. 3. Formation energies (ΔE_{form}) for V_{Si} in different charged states as a function of the Fermi energy level (electronic chemical potential) in SiC/AlN-H at the S1 (interior) and S2 (interface) sites within the SiC/AlN-H NW. The electronic chemical potential (Fermi energy level) is given with respect to the valence band maximum. The formation energies are calculated assuming carbon-rich conditions. The favorable doping conditions at which the negatively charged state ($q = -1$) of the defect is stable, are highlighted.

Silicon vacancy in passivated SiC/AlN-H NW

As discussed in the previous section, the hydrogenation of the surface of our extremely thin AlN-shell allowed us to emulate the behavior of experimentally-relevant thicknesses of AlN shells [26]. In doing so, we also remedied the excessive structural changes at the SiC-AlN interface, which are artifacts of the skin-contraction effects and not due to lattice mismatch. Our next step was to study

properties of V_{Si}^{-1} at the S1 and S2 sites in SiC/AlN-H. Before presenting our results for V_{Si}^{-1} at these sites, it is instructive to see how the presence of the AlN shell may change the charge state stability. To do so, we calculated the defect formation energies as defined in earlier works [23, 40] for V_{Si} at the S1 (interior) and S2 (interface) sites within the SiC/AlN-H NW. Figures 3 (a) and (b) are plots of defect formation energies vs electronic chemical potential (Fermi energy) referenced to the valence band maximum. These results are obtained under carbon-rich (i.e. silicon-poor) conditions, which would be the growth condition that favors formation of silicon vacancies. The highlighted regions reveal that the bright, negatively-charged state of V_{Si} is stable over a considerable range of n-doping for both S1 and S2 sites, although the favorable range for the S2-site is shifted to lower values of n-doping than that for S1. We would like to point out that our results for V_{Si} at S1-site [see Fig. 3(a)] are similar to those obtained for simple adsorbate-passivated SiC NW [23] and to those reported for monovacancies in bulk 4H-SiC within the HSE06 approximation [41, 42]. We also find that the $q = -2$ charge state becomes favorable for a much larger doping range for the defect at S2, which might become an important consideration for highly n-doped SiC.

V_{Si}^{-1} at the S1 (interior) site in SiC/AlN-H NW

The singly charged V_{Si}^{-1} defect at the interior site, S1, has a total of five electrons in the dangling bonds left behind by the monovacancy. It is a spin-3/2 defect, just as in bulk SiC [7, 22, 43, 44]. Figures 4(a)-(d) give the details of the electronic structure for this defect. Figure 4(a) is a plot of TDOS (in gray) of the defective SiC/AlN-H NW, along with the projected DOS contributed by the SiC core (in gold), AlN shell (in thin black line) and the four NN carbon-atoms, C_{NN} 's surrounding the defect (in blue). The plot clearly shows that the defect creates localized defect states in the band gap. The DOS contributed by SiC shows that the defect states are contributed by the core with negligible contribution from the AlN shell. The DOS contribution from the four C_{NN} 's and the isosurface plot for the spin density [$\Delta\rho^{spin} = \rho^{\uparrow} - \rho^{\downarrow}$] in Fig. 4(b) further shows that the most of the spin-3/2 of the defect comes from the unpaired electrons in the dangling bonds associated with the carbon atoms surrounding the defect. To understand the origin of spin-3/2 for the defect, we show the energy-level diagram in Fig. 4(c). The defective NW structure has the C_s symmetry, unlike the C_{3v} symmetry for the defect in the bulk [22, 23], and thus, all of the defect states are singlets. The five electrons in the dangling bonds fill the “atomic-like” localized defect states such that there are three more electrons in the spin-up channel (majority-spin) than the spin-down channel (minority

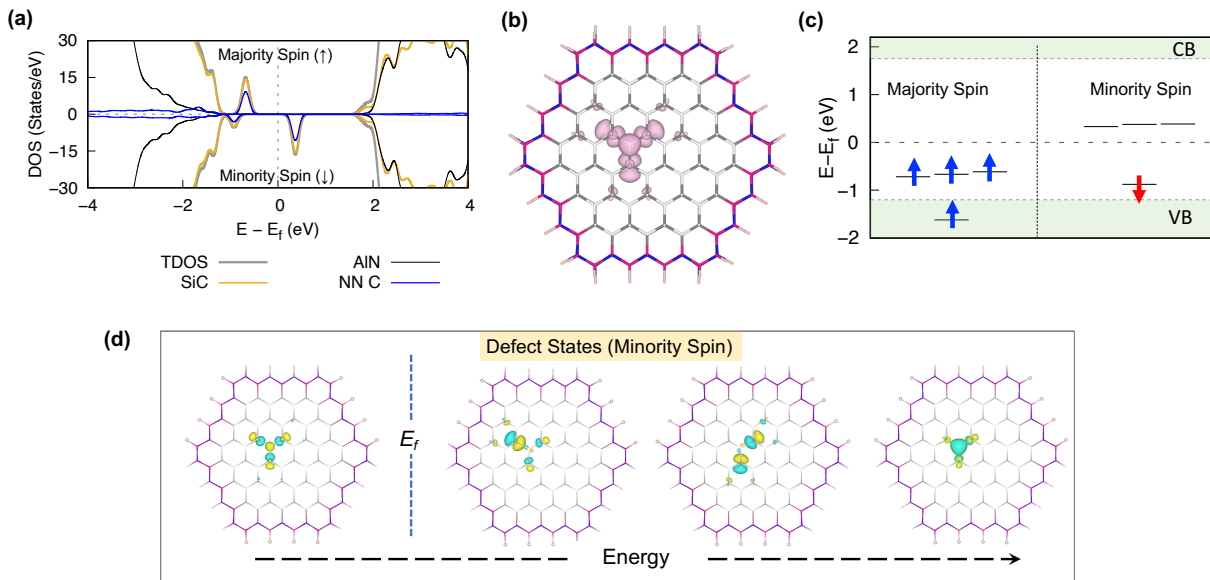


FIG. 4. SiC/AlN-H NW with a V_{Si}^{-1} defect in the interior (S1 site). (a) Total density of states (TDOS) in thick gray line, along with the DOS contributed by the SiC core (in gold), AlN shell (thin black line) and the four NN carbon-atoms (in blue). (b) Spin density $[\Delta\rho^{spin}]$ isosurface plot for the monovacancy at the S1 site, showing that the most of the spin-3/2 of the defect comes from the unpaired electrons in the sp^3 -hybridized $2s$ and $2p$ orbitals of the carbons surrounding the defect. Here, $\Delta\rho^{spin} = \rho^\uparrow - \rho^\downarrow$ is the difference in the spin-up and spin-down charge densities. (c) Energy-level diagram, showing the positions of the defect states in majority spin (spin-up) and minority spin (spin down) channels at the Γ -point. The optically-active defect states in the minority spin channel are well-separated from the valence band (VB) and conduction band (CB) states. (d) The charge density plots of the optically-active empty and filled state for SiC/AlN-H NW at the Γ -point. Yellow (blue) color corresponds to positive (negative) isovalues.

spin), resulting in the spin-3/2 for the defect.

The optical excitation happens between the filled and the empty defect states in the spin-down channel. Figure 4(d) shows the charge density plots for these optically-active empty and filled states. The calculated value of the ZPL is 1.12 eV, which differs from the bulk ZPL-value of 1.19 eV by about 75 meV. As discussed in earlier works [22, 23], the difference in ZPL for a defect close to the surfaces and/or interfaces can be attributed to several inter-connected factors, with the most significant being: (i) local strains, (ii) differences in Stokes shift, which result from different structural relaxation around the defect upon photoexcitation, and (iii) different placements and hence gaps between the optically-active defect states, resulting in different absorption energies. To estimate the strain-induced change in the ZPL, we used the experimentally-determined strain-coupling parameter, $1130 \text{ meV}(\text{strain})^{-1}$, for strain in the basal direction [17]. The bond lengths along the basal plane at the S1-site are 0.39% longer as compared to the ideal basal distance. This yields a ZPL-change of 4.38 meV, showing that strain is relatively less important in changing the ZPL. The Stokes shift, given by $E_B - E_C$ in Fig. 1(c), is calculated to be 122.3 meV for the defect at S1, while it is 104.9 meV for the defect in the bulk material. The 17.4 meV difference in the Stokes shift accounts for some of the calculated ZPL shift. In the case of V_{Si}^{-1}

at the S1-site in the SiC/AlN-H NW, the largest contributor to the ZPL-shift is from the differences in vertical absorption energies [$E_B - E_A$ in Fig. 1(c)] for the defect at the S1 site (1.24 eV) and for the bulk (1.30 eV), with a 57.89 meV decrease in the calculated value of $E_B - E_A$ for the defect in core-shell NW as compared to the bulk. To see the influences of the AlN-shell on the optical properties of the interior defect, we also calculated the optical properties of V_{Si}^{-1} at an interior-site in the SiC-H NW. We find that the ZPL for this defect (1.16 eV) is much closer to that for the bulk SiC, with a 30 meV difference in the ZPL. For the monovacancy in the interior site of SiC-H NW, the contributions to the ZPL-shift from strain, changes in Stokes shift and the vertical excitation are found to be 1.57 meV, 11.77 meV and 16.87 eV, respectively. Hence, the largest change produced by AlN shell is in the placement of the defect states within the band gap (as compared to a SiC-H NW), owing to the changes in the electronic structure properties upon creating a core-shell NW.

V_{Si}^{-1} at the S2 (interface) site in SiC/AlN-H NW

At the S2 site, a negatively charged silicon vacancy is surrounded by three nearest neighbor carbons and one nitrogen atom from the shell [see Figure 1(b)]. One might

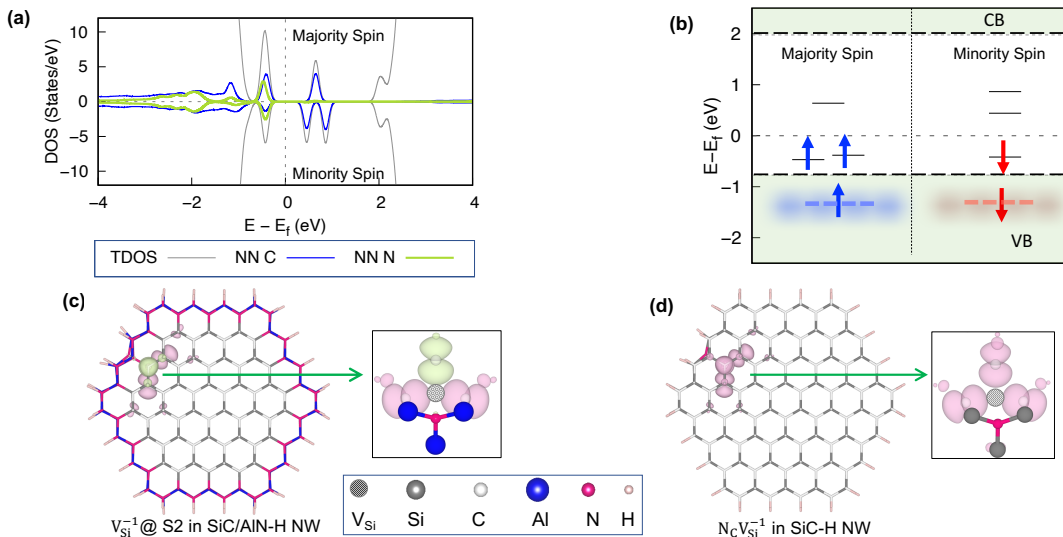


FIG. 5. SiC/AlN-H NW with a V_{Si}^{-1} defect at the core-shell interface (S2 site). (a) Total density of states (TDOS), along with the DOS contributed by the nearest neighboring (NN) atoms surrounding the defect. The latter include contributions from the $2s$ and $2p$ orbitals of the three C_{NN} (in blue) and N_{NN} (in green). (b) Energy-level diagram, showing the positions of the in-gap defect states in majority spin (spin-up) and minority spin (spin down) channels at the Γ -point. The lowest defect states, which are resonant with the valence band (VB), mix with the VB states and can no longer be uniquely identified. They are included for the sake of completeness. (c) Spin density plot for the monovacancy at the S2 site. Pink (green) color corresponds to positive (negative) isovalues. Also shown is a close-up of the spin density plot (side-view), consisting of the three C_{NN} 's and the N_{NN} -atom, along with the Al atoms bonded to N_{NN} . (d) Spin density isosurface plot for the negatively charged $N_C V_{Si}^{-1}$ -center in the H-SiC NW [at the same site as the defect in (c)]. The close-up (side-view) shows C_{NN} 's and the N_{NN} -atom, along with the Si atoms bonded to N_{NN} .

naïvely expect this defect to behave like a negatively charged NV-center in SiC, wherein a substitutional nitrogen replaces one of the nearest neighbor carbons of the silicon monovacancy. In bulk 2H-SiC, such an NV center, with an N-atom substituting a basal C-atoms, is a spin-1 defect. However, for the negatively charged defect at S2 we found two solutions – a spin-1/2 (low-spin) ground state solution and a spin-3/2 (high-spin) metastable solution. The latter was higher in energy as compared to the low-spin state solution by 163.30 meV. Interestingly, neither of the two solutions can be explained by assuming that the defect at the S2-site has a total of six electrons in four dangling bonds surrounding the monovacancy. In fact, a singly negatively-charged defect behaves as if it has a total of five electrons in the defect states. In what follows, we will concentrate on the lower-energy spin-1/2 solution for the interfacial defect, but similar arguments apply to the metastable solution as well.

We first concentrate on explaining the calculated electronic structure to explain the spin-1/2 of the defect and then tackle the question: “where is the sixth electron?” In Fig. 5(a), we plot the total and the partial DOS plots for the spin-1/2 defect at the interface, showing that the defect introduces very localized (sharp) defect states in the band gap. The DOS contributions from the $2s$ and $2p$ orbitals of the NN carbons atoms (in blue) and nitrogen atom (in green) show that the in-gap sharp states originate in the dangling bonds on the surrounding atoms.

The energy-level diagram is shown in Fig. 5(b). The defect states resonant with VB are shown as “fuzzy” lines as these defect states hybridize with the states in the VB and their position can no longer be uniquely given. A comparison with the energy level diagram for the interior defect [Fig. 4(c)] shows that the three nearly-degenerate defect states of the interior defect have undergone larger crystal field splitting at the interface, with the distribution of the five electrons resulting in net spin-1/2 for the interfacial defect. The spin density for the defect at the interface is shown in Figure 5(c). Pink (green) color corresponds to positive (negative) isovalues. The magnetic moment of the axial NN carbon is antiferromagnetic aligned to the moments of the NN carbons along the basal plane, resulting in the net spin-1/2 for the defect. The close-up of the spin density plot (side-view) shows only the three C_{NN} atoms and N_{NN} atom, along with the Al atoms bonded to the N_{NN} -atom. The three Al atoms are shown to highlight that, although nominally a negatively-charged NV center, this defect has a different chemical environment as compared to the same defect in SiC bulk or SiC NW without an AlN shell. To demonstrate that the antiferromagnetic alignment is not a result of proximity to the surface, we created a negatively charged $N_{\text{basal-C}}V_{Si}$ defect center (subsequently referred to as the “NV-center”) in a SiC-H NW at the same site. We find that the near-surface, negatively-charged NV center in SiC-H NW is a spin-1 defect (similar to the NV-center

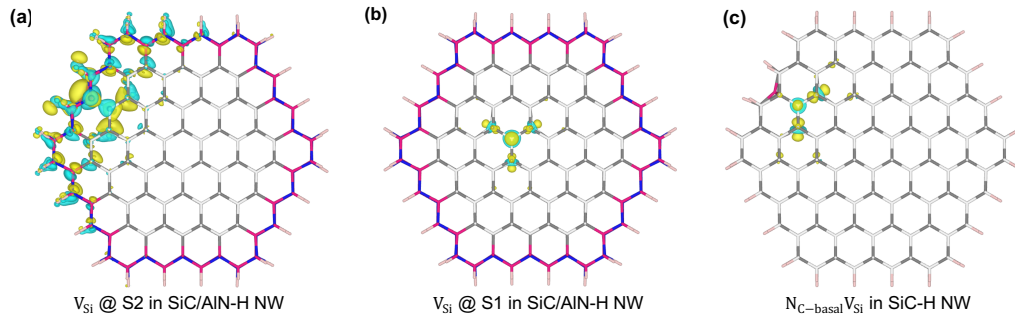


FIG. 6. Charge density difference [$\Delta\rho = \rho^{q=-1} - \rho^{q=0}$] for: (a) V_{Si} at the S2 (interface) site in the SiC/AlN-H NW, showing how the additional charge gets delocalized over a large region, including parts of the AlN shell and SiC core, (b) V_{Si} at the S1 (interior) site in the SiC/AlN-H NW, and (c) an NV center in the SiC-H NW, with the last two cases showing the localized nature of the additional charge. Yellow (blue) color corresponds to regions with charge accumulation (depletion).

in the bulk SiC) with a spin-density distribution shown in Fig. 5(d). Hence, neither the nanostructuring of SiC, nor the proximity to the surface are responsible for the behavior of the interfacial defect in SiC/AlN-H NW.

In order to answer the question posed in the previous paragraph (“where is the sixth electron?”), we calculated the charge-density differences between the singly-charged and neutral defects [$\Delta\rho = \rho^{q=-1} - \rho^{q=0}$] for three systems: V_{Si} at the S2 (interface) site in SiC/AlN-H NW (effectively, an NV center), V_{Si} at the S1 (interior) site in SiC/AlN-H NW, and an NV center in a SiC-H NW. The charge densities for the neutral charge states of all three defects were calculated with the respective equilibrium geometries obtained for the three negatively-charged structures. Figures 6(a)-(c) are the plots of the charge density differences for the three systems. Yellow (blue) color corresponds to regions with charge accumulation (depletion). Overall, Figs 6(a)-(c) show the sense in which charge is redistributed upon addition of an electron to the respective neutral defects. The charge density differences for the monovacancy at S2 in Fig. 6(a) shows that the electron added to the neutral defect at S2 does not get localized at the defect site. It is instead distributed over a large region, including the AlN shell. One may suspect that this is either due to the nanostructuring of SiC itself or due to the proximity of the defect to the surface. That this is not the case can be seen in the highly-localized charge redistribution upon the addition of an electron for the other two structures shown in Figs 6(b) and (c). Hence, we find that the defect at S2 is fundamentally different from the other two defects and we attribute this to the different chemical environment of the defect at the AlN-SiC interface. Interestingly, the interfacial defect acquires a spin-1 ground state when it is doubly-negatively charged. This charge state becomes stable for the V_{Si} at the S2 site for highly negatively doped NW as seen in Fig. 3(b). In our nanostructure, both $q = -1$ and $q = -2$ charge states of the interfacial defect have a spin-active ground state, with the magnetic structures being more stable than the non-magnetic

structures by 387.03 meV and 415.29 meV, respectively. The ZPLs for the singly and doubly charged monovacancies at the S2-site are 0.68 eV and 0.77 eV, respectively. The latter is comparable to the ZPL of 0.84 eV for the spin-1 NV^{-1} -center (with N substituting a basal carbon) in bulk 2H-SiC. The difference in the ZPLs of the two spin-1 defects originates mostly from the much larger Stokes shift for the doubly-charged interfacial monovacancy (158.48 meV) as compared to that for the singly-charged NV-center in bulk 2H-SiC (82.23 meV).

CONCLUSION

The loss of photostability of near-surface, defect-based quantum emitters within nanostructured semiconductors is a severe bottleneck for their successful deployment in different quantum technologies. In this work, we have demonstrated that the core-shell structure, which consists of a SiC core passivated with an AlN shell, can effectively remove the detrimental surface states from the band gap of the nanostructured SiC host, elucidating the findings of an earlier experimental work [26]. In such a core-shell model, the AlN shell replaces simple atomic/molecular adsorbates, which will otherwise be used to passivate the surface states but are limited by their lack of long-term chemical and thermal stability. The presence of an AlN shell not only resolves the issue of charge-state instability of the near-surface V_{Si}^{-1} defect, it also restores the optical properties of this spin-3/2 defect. In addition, we identify a V_{Si} -related defect at the interface of the SiC core and the AlN shell. This interfacial defect is nominally similar to the NV-center in SiC (with nitrogen along the basal plane), but displays different spin and optical properties from an NV-center in SiC due to its distinct chemical environment at the interface. Our atomistic study of defects in SiC/AlN-H NW shows a promising means of resolving the optical stability issues of quantum emitters in nanostructured host semiconductors via creation of core-shell structures

or growth/deposition of an appropriate semiconductor as a passivation layer on thin films of host semiconductors.

Acknowledgements: We acknowledge support by the National Science Foundation under NSF grant number DMR-1738076 and the STC Center for Integrated Quantum Materials under NSF Grant number DMR-1231319. This work used the Expanse and Bridges2 clusters at SDSC and PSC, respectively, through allocation PHY180014 from the Advanced Cyberinfrastructure Co-ordination Ecosystem: Services & Support (ACCESS) program, which is supported by National Science Foundation grants No. 2138259, No. 2138286, No. 2138307, No. 2137603, and No. 2138296.

Author Contributions: P.D. conceived and directed the study. C.A.S.N. and P.D. performed the calculations. P.D. wrote the final manuscript with inputs from the first draft written by C.A.S.N. Both authors proof-read and reviewed the final revision of the manuscript.

-
- [1] D. J. Christle, A. L. Falk, P. Andrich, P. V. Klimov, J. U. Hassan, N. T. Son, E. Janzzén, T. Ohshima, and D. D. Awschalom, *Nature Materials* **14**, 160 (2015), URL <https://doi.org/10.1038/nmat4144>.
- [2] F. Fuchs, B. Stender, M. Trupke, D. Simin, J. Pflaum, V. Dyakonov, and G. V. Astakhov, *Nature Communications* **6**, 7578 (2015), URL <https://doi.org/10.1038/ncomms8578>.
- [3] A. L. Falk, B. B. Buckley, G. Calusine, W. F. Koehl, V. V. Dobrovitski, A. Politi, C. A. Zorman, P. X.-L. Feng, and D. D. Awschalom, *Nature Communications* **4**, 1 (2013), URL <https://doi.org/10.1038/ncomms2854>.
- [4] M. Widmann, S.-Y. Lee, T. Rendler, N. T. Son, H. Fedder, S. Paik, L.-P. Yang, N. Zhao, S. Yang, I. Booker, et al., *Nature Materials* **14**, 164 (2015), URL <https://doi.org/10.1038/nmat4145>.
- [5] H. Seo, A. L. Falk, P. V. Klimov, K. C. Miao, G. Galli, and D. D. Awschalom, *Nature Communications* **7**, 12935 (2016), URL <https://doi.org/10.1038/ncomms12935>.
- [6] R. Nagy, M. Niethammer, M. Widmann, Y.-C. Chen, P. Udvarhelyi, C. Bonato, J. U. Hassan, R. Karhu, I. G. Ivanov, N. T. Son, et al., *Nature Communications* **10**, 1 (2019), URL <https://doi.org/10.1038/s41467-019-09873-9>.
- [7] S. G. Carter, O. O. Soykal, P. Dev, S. E. Economou, and E. R. Glaser, *Physical Review B* **92**, 161202 (2015), URL <https://link.aps.org/doi/10.1103/PhysRevB.92.161202>.
- [8] M. N. Gadalla, A. S. Greenspon, R. K. Defo, X. Zhang, and E. L. Hu, *Proceedings of the National Academy of Sciences* **118** (2021), URL <https://doi.org/10.1073/pnas.2021768118>.
- [9] S. Majety, V. A. Norman, L. Li, M. Bell, P. Saha, and M. Radulaski, *Journal of Physics: Photonics* **3**, 034008 (2021), URL <https://doi.org/10.1088/2515-7647/abfdca>.
- [10] A. L. Crook, C. P. Anderson, K. C. Miao, A. Bourassa, H. Lee, S. L. Bayliss, D. O. Bracher, X. Zhang, H. Abe, T. Ohshima, et al., *Nano Letters* **20**, 3427 (2020), URL <https://doi.org/10.1021/acs.nanolett.0c00339>.
- [11] D. O. Bracher, X. Zhang, and E. L. Hu, *Proceedings of the National Academy of Sciences* **114**, 4060 (2017), URL <https://doi.org/10.1073/pnas.1704219114>.
- [12] R. Nagy, M. Widmann, M. Niethammer, D. B. Dasari, I. Gerhardt, Ö. O. Soykal, M. Radulaski, T. Ohshima, J. Vučković, N. T. Son, et al., *Physical Review Applied* **9**, 034022 (2018), URL <https://doi.org/10.1103/PhysRevApplied.9.034022>.
- [13] D. M. Lukin, C. Dory, M. A. Guidry, K. Y. Yang, S. D. Mishra, R. Trivedi, M. Radulaski, S. Sun, D. Vercruysee, G. H. Ahn, et al., *Nature Photonics* **14**, 330 (2020), URL <https://doi.org/10.1038/s41566-019-0556-6>.
- [14] M. Radulaski, M. Widmann, M. Niethammer, J. L. Zhang, S.-Y. Lee, T. Rendler, K. G. Lagoudakis, N. T. Son, E. Janzen, T. Ohshima, et al., *Nano Letters* **17**, 1782 (2017), URL <https://doi.org/10.1021/acs.nanolett.6b05102>.
- [15] Z. Yuan, M. Fitzpatrick, L. V. H. Rodgers, S. Sangtawesin, S. Srinivasan, and N. P. de Leon, *Physical Review Research* **2**, 033263 (2020), URL <https://link.aps.org/doi/10.1103/PhysRevResearch.2.033263>.
- [16] S. Sangtawesin, B. L. Dwyer, S. Srinivasan, J. J. Allred, L. V. Rodgers, K. De Greve, A. Stacey, N. Dontschuk, K. M. O'Donnell, D. Hu, et al., *Physical Review X* **9**, 031052 (2019), URL <https://doi.org/10.1103/PhysRevX.9.031052>.
- [17] G. C. Vásquez, M. E. Bathen, A. Galeckas, C. Bazioti, K. M. Johansen, D. Maestre, A. Cremades, Ø. Prytz, A. M. Moe, A. Y. Kuznetsov, et al., *Nano Letters* **20**, 8689 (2020), URL <https://doi.org/10.1021/acs.nanolett.0c03472>.
- [18] J. N. Neethirajan, T. Hache, D. Paone, D. Pinto, A. Denisenko, R. Stöhr, P. Udvarhelyi, A. Pershin, A. Gali, J. Wrachtrup, et al., *Nano Letters* **23**, 2563 (2023), URL <https://doi.org/10.1021/acs.nanolett.2c04733>.
- [19] M. Kaviani, P. Deák, B. Aradi, T. Frauenheim, J.-P. Chou, and A. Gali, *Nano Letters* **14**, 4772 (2014), URL <https://doi.org/10.1021/nl501927y>.
- [20] S. Li, J.-P. Chou, J. Wei, M. Sun, A. Hu, and A. Gali, *Carbon* **145**, 273 (2019), ISSN 0008-6223, URL <https://www.sciencedirect.com/science/article/pii/S0008622319300168>.
- [21] R. Löfgren, R. Pawar, S. Öberg, and J. A. Larsson, *New Journal of Physics* **21**, 053037 (2019), URL <https://dx.doi.org/10.1088/1367-2630/ab1ec5>.
- [22] T. Joshi and P. Dev, *PRX Quantum* **3**, 020325 (2022), URL <https://link.aps.org/doi/10.1103/PRXQuantum.3.020325>.
- [23] C. A. Sayou Ngoms, T. Joshi, and P. Dev, *Phys. Rev. Mater.* **8**, 056202 (2024), URL <https://link.aps.org/doi/10.1103/PhysRevMaterials.8.056202>.
- [24] L. M. Struck and M. P. D'Evelyn, *Journal of Vacuum Science & Technology A* **11**, 1992 (1993), ISSN 0734-2101, https://pubs.aip.org/avs/jva/article-pdf/11/4/1992/7371106/1992_1_online.pdf, URL <https://doi.org/10.1116/1.578397>.
- [25] R. E. Thomas, R. A. Rudder, and R. J. Markunas, *Journal of Vacuum Science & Technology A* **10**, 2451 (1992), ISSN 0734-2101, URL <https://doi.org/10.1116/1.578397>.

- 1116/1.577983.
- [26] M. J. Polking, A. M. Dibos, N. P. de Leon, and H. Park, *Advanced Materials* **30**, 1704543 (2018), URL <https://onlinelibrary.wiley.com/doi/abs/10.1002/adma.201704543>.
- [27] P. Giannozzi, S. Baroni, N. Bonini, M. Calandra, R. Car, C. Cavazzoni, D. Ceresoli, G. L. Chiarotti, M. Cococcioni, I. Dabo, et al., *Journal of Physics: Condensed Matter* **21**, 395502 (19pp) (2009), URL <http://www.quantum-espresso.org>.
- [28] P. Giannozzi, O. Andreussi, T. Brumme, O. Bunau, M. B. Nardelli, M. Calandra, R. Car, C. Cavazzoni, D. Ceresoli, M. Cococcioni, et al., *Journal of Physics: Condensed Matter* **29**, 465901 (2017), URL <http://stacks.iop.org/0953-8984/29/i=46/a=465901>.
- [29] D. Vanderbilt, *Phys. Rev. B* **41**, 7892 (1990), URL <https://link.aps.org/doi/10.1103/PhysRevB.41.7892>.
- [30] J. P. Perdew and W. Yue, *Physical Review B* **33**, 8800 (1986), URL <https://link.aps.org/doi/10.1103/PhysRevB.33.8800>.
- [31] J. P. Perdew, K. Burke, and M. Ernzerhof, *Physical Review Letters* **77**, 3865 (1996), URL <https://link.aps.org/doi/10.1103/PhysRevLett.77.3865>.
- [32] J. Heyd, G. E. Scuseria, and M. Ernzerhof, *The Journal of Chemical Physics* **118**, 8207 (2003), <https://doi.org/10.1063/1.1564060>.
- [33] J. Heyd, G. E. Scuseria, and M. Ernzerhof, *The Journal of Chemical Physics* **124**, 219906 (2006), <https://doi.org/10.1063/1.2204597>.
- [34] A. J. Cohen, P. Mori-Sánchez, and W. Yang, *Science* **321**, 792 (2008), URL <http://www.jstor.org/stable/20144547>.
- [35] H. J. Monkhorst and J. D. Pack, *Physical Review B* **13**, 5188 (1976), URL <https://link.aps.org/doi/10.1103/PhysRevB.13.5188>.
- [36] A. Gali, E. Janzén, P. Deák, G. Kresse, and E. Kaxiras, *Phys. Rev. Lett.* **103**, 186404 (2009), URL <https://link.aps.org/doi/10.1103/PhysRevLett.103.186404>.
- [37] P. Dev, *Physical Review Research* **2**, 022050(R) (2020), URL <https://link.aps.org/doi/10.1103/PhysRevResearch.2.022050>.
- [38] S. K. Narayanan and P. Dev, *ACS Applied Nano Materials* **6**, 3446 (2023), URL <https://doi.org/10.1021/acsnm.2c05233>.
- [39] W. J. Huang, R. Sun, J. Tao, L. D. Menard, R. G. Nuzzo, and J. M. Zuo, *Nature Materials* **7**, 308 (2008), URL <https://doi.org/10.1038/nmat2132>.
- [40] T. Tanaka, K. Matsunaga, Y. Ikuhara, and T. Yamamoto, *Phys. Rev. B* **68**, 205213 (2003), URL <https://link.aps.org/doi/10.1103/PhysRevB.68.205213>.
- [41] K. Szász, V. Ivády, I. A. Abrikosov, E. Janzén, M. Bockstedte, and A. Gali, *Phys. Rev. B* **91**, 121201 (2015), URL <https://link.aps.org/doi/10.1103/PhysRevB.91.121201>.
- [42] L. Gordon, A. Janotti, and C. G. Van de Walle, *Phys. Rev. B* **92**, 045208 (2015), URL <https://link.aps.org/doi/10.1103/PhysRevB.92.045208>.
- [43] Ö. Soykal, P. Dev, and S. E. Economou, *Physical Review B* **93**, 081207 (2016), URL <https://doi.org/10.1103/PhysRevB.93.081207>.
- [44] S. E. Economou and P. Dev, *Nanotechnology* **27**, 504001 (2016), URL <https://doi.org/10.1088/0957-4484/27/50/504001>.